Publications of the Astronomical Society of Japan, 2025, **00**, 1–7
doi: 10.1093/pasj/xxx000
Advance access publication date:

The highest resolution unified rotation curve of the Galaxy decomposed into the nucleus, core, bulge, disk, and dark halo components - URC26 -

Yoshiaki SOFUE[1]

[1]Institute of Astronomy, The University of Tokyo, 2-21-1 Mitaka, Tokyo 181-8588, Japan
*E-mail: sofue@ioa.s.u-tokyo.ac.jp

ORCID: 0000-0002-4268-6499

Abstract

We present the unified rotation curve of the Milky Way with the highest resolution and most complete sampling from the central super massive black hole (SMBH) to the outermost halo up to ~ 300 kpc. We decompose the URC into the following five mass components: 1. the fixed central SMBH, 2. massive core $(a_i,\ M_i) = (181\ \mathrm{pc},\ 4.7\times10^7 M_\odot)$, 3. bulge $(358\ \mathrm{pc},\ 1.3\times10^{10} M_\odot)$, 4. disk $(5.6\ \mathrm{kpc},\ 1.03\times10^{11} M_\odot)$, and 5. dark halo (DH) fitted by the Navarro-Frenk-White model with the scale radius $h\sim11$ kpc, critical radius $R_{200}\sim36$ kpc, critical DH and total masses $M_{200}^{\rm DM}\sim2\times10^{11}M_\odot$ and $M_{200}\sim3\times10^{11}M_\odot$ for $H_0=71$ km s^{-1}/ Mpc^{-1}. The scale radii and masses of the five components show a linear scaling relation expressed by $M_i\sim10^7 M_\odot (a_i/1\ \mathrm{pc})^{1.1}$ with i being the i-th component. The dark matter density near the Sun due to the dark halo is estimated to be $\sim$0.24 to 0.28 GeV cm^{-3}.

Keywords: galaxies: individual (Milky Way) — galaxies: rotation curve — Galaxy: kinematics and dynamics — galaxies: Cosmology – dark matter

1 Introduction

Rotation curve (RC) is the most fundamental tool for measuring the dynamical mass and its distribution in the Galaxy under the assumption that the galaxy is rotating around its polar axis (Sofue and Rubin 2001; Sofue 2017; Salucci 2019; Sofue 2020).

In our earlier papers (Sofue et al. 2009; Sofue 2012; Sofue 2013) we have constructed "unified RCs" of the Galaxy from the nucleus to a half way to M31 including the outer halo by combining the existing rotation data in the decades from 1980's to 2000's. We have also deconvolved the RC into several mass components to obtain fundamental parameters such as the total mass and scale size of each component, as well as the local density of dark matter (DM) (Sofue 2013; Sofue 2020).

In this paper, we revise the URC of the Milky Way by employing the most recent data about Galactic rotation. We integrate the current RCs determined individually for the Galactic Center by the ALMA molecular line survey of the central molecular zone (CMZ) (Longmore et al. and ACES Team 2025; Sofue et al. 2025), the inner disk using the CO and HI-line surveys of the Galactic plane (Sofue & Kohno 2025), the stellar disk by trigonometry of maser sources using VERA (VERA Collaboration et al. 2020) and VLBA (Reid et al. 2019), the disk stars by GAIA trigonometry (Eilers et al. 2019), and 3D velocities of globular clusters and dwarf galaxies with GAIA (Jiao et al. 2023; Sylos Labini 2024). We adopt the Galactic constants $R_0=8.18$ kpc (Gravity Collaboration et al. 2019) and $\Theta_0=235.1$ km s^{-1} (Sofue & Kohno 2025).

2 Construction of URC26

2.1 Central black hole

The rotation curve around the central supermassive black hole (SMBH) located at the nucleus (Sgr A*) with a mass of $M_1=4.0\times10^6 M_\odot$ (Ghez et al. 2008; Gillessen et al. 2009) is represented by the Keplerian law.

2.2 Central Molecular Zone (CMZ)

We have recently determined the RC in the CMZ using the ACES survey data (Longmore et al. and ACES Team 2025) by applying the terminal velocity method to the longiutde-velocity diagrams (LVD) of the CS $(J=2-1)$-line emission from the molecular gas in the CMZ and the H40α-line from the ionized gas in the minispiral (Sofue et al. 2025). Figure 1 shows the RC inside $R\sim120$ pc. The entire CMZ has a nearly flat RC at $V_{\rm rot}\sim100$ km s^{-1} associated with a peak around $R\sim5$ pc. The innermost $V_{\rm rot}$ within $R\lesssim1$ pc increases toward the nucleus, obeying the Keplerian law due to the central SMBH.

2.3 Gas disk by terminal velocities of CO and HI lines

Inside the solar circle ($-90^\circ\le l\le90^\circ$), the rotation velocity $V(R)$ at the galacto-centric distance $R=R_0\sin l$ is calculated simply by correcting the terminal velocity $V_{\rm term}$ for the circular motion of the LSR (local standard of rest) at the Sun:

$$V_{\rm rot}(R)=V_{\rm term}+\Theta_0\sin l. \quad (1)$$

In figure 1 we show the inner RC obtained recently by Sofue & Kohno (2025), applying TVM to CO and HI line survey data of

Received: , **Accepted:**

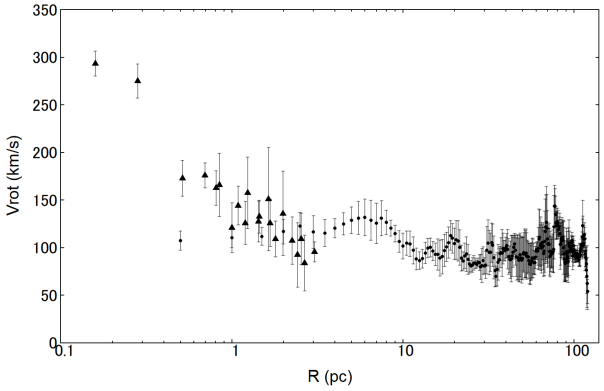

Fig. 1. Rotation curve of the CMZ in the central 120 pc obtained by terminal velocity method for H40α (triangles) and CS ($J=2-1$) (dots) lines in semilogarithmic scaling (Sofue et al. 2025). Alt text: Rotation curve of the Galactic Center.

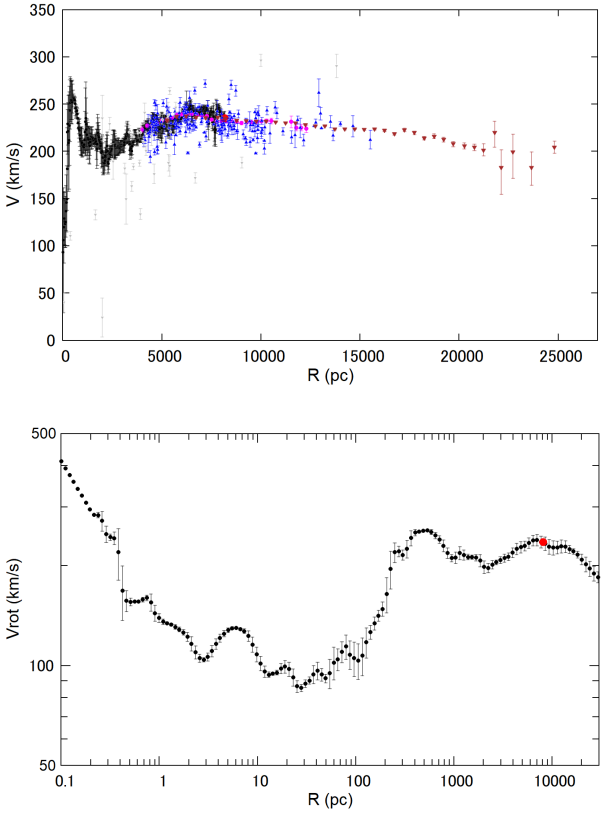

Fig. 2. [Top] RC up to 30 kpc by combining the inner RC of the gas disk using the terminal velocity method (black dots) (Sofue & Kohno 2025), trigonometry of maser sources with VERA (blue dots) (VERA Collaboration et al. 2020) and VLBA (magenta dots) (Reid et al. 2019), and disk stars by GAIA DR3 (brown triangles) (Jiao et al. 2023) by combining the RCs in figures 1 and 2. [Bottom] Same, but with equal logarithmic radius increment after Gaussian running averaging. The big dot marks the Sun at $(8.2\,\mathrm{kpc},\ 235\ \mathrm{km\,s^{-1}})$. Points at $R\leq 0.2$ pc are Keplerian circular velocities calculated for the central SMBH of $4\times10^6 M_\odot$. Alt text: Unified rotation curve from the GC to halo.

the Galactic plane (Dame et al. 2001; HI4PI Collaboration et al. 2016; Umemoto et al. 2017; Braiding et al. 2015; Cubuk et al. 2023).

2.4 Stellar disk by VLBI trigonometry of maser sources

Recent trigonometric measurements of maser sources using VERA (VLBI exploration of radio astrometry) (VERA Collaboration et al. 2020) and VLBA (very long baseline array) (Reid et al. 2019) have provided accurate 3D motions of the sources in the Galactic disk, which yielded circular rotational rotation curves at high accuracy. These results were combined with the inner RC from the terminal velocity to yield an RC from the Galactic Center to the halo at $R\sim15$ kpc. In figure 2 we plot the circular velocities of maser sources from VERA by blue triangles and those by VLBA measurements by magenta dots.

2.5 Stellar disk and halo by GAIA trigonometry

The GAIA mission has provided proper motions of billions of stars in the Milky Way, and yielded high accuracy rotation curves of the mid to outer Galactic disk at $R\sim8$ to 25 kpc (Eilers et al. 2019; Jiao et al. 2023; Sylos Labini 2024). We plot the circular velocities from GAIA DR3 by the inverse triangles in figure 2.

2.6 RC of the halo up to ~300 kpc by GAIA trigonometry of globular clusters and dwarf galaxies

In order to construct a rotation curve of the Galactic halo up to several hundred kpc, we employ the GAIA trigonometric measurements of globular clusters (Vasiliev & Baumgardt 2021; Wang et al. 2022) and dwarf galaxies (Li et al. 2021; Hammer et al. 2021; Hammer et al. 2023). Circular rotation velocities using globular clusters are presented by Wang et al. (2022), which cover from $R\sim25$ to ~100 kpc. For larger radii from $R\sim25$ to ~300 kpc, we introduce a "pseudo" rotation velocity (Sofue 2013) of dwarf galaxies defined by

$$V_{\rm rot}=\eta\sqrt{v_{\rm RA}^2+v_{\rm Dec}^2+v_{\rm radial}^2}. \tag{2}$$

Here, v_i ($i=$RA, Dec, radial) are the velocities calculated for the proper motions and radial velocity with GAIA and η is a conversion factor of the 3D velocity to a pseudo circular velocity at the same radius. We assume $\eta\sim1/\sqrt{2}$, considering that the dwarfs are half a way to their apocenters and the orbital inclinations to the line of sights are random. We also examine a case with $\eta=1$, which will yield the upper limit of the circular velocity. This factor could vary between $\eta\sim1$ and $\sim1/\sqrt{3}$, depending on the dynamical condition of the halo. This means that the dark halo mass estimation in this paper includes a systematic error of a factor of ~2.

2.7 URC26: Unified RC from the GC to outermost halo by Gaussian running averaging

We then construct a unified RC (URC) by taking Gaussian running average (GRA) of the circular velocities $V(R_i)$ measured at $R=R_i$ for the i-th data points by the individual methods. The GRA value of V at a radius R is calculated by

$$V(R)=\frac{\int_{i=1}^{N}V_i w_i}{\int_{i=1}^{N}w_i} \tag{3}$$

and

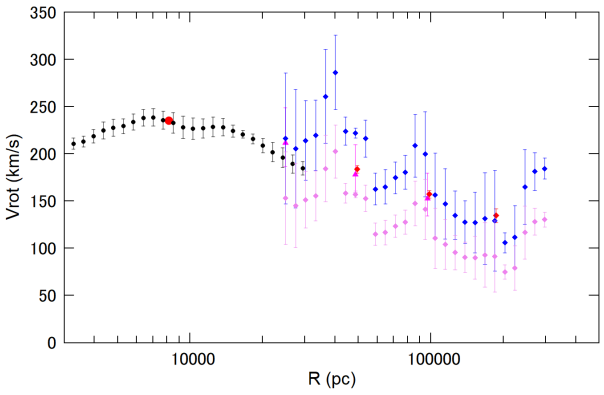

Fig. 3. GAIA outer rotation curves by Gaussian running average of the 3D velocities inferred from proper motions and radial velocities of globular clusters (magenta and red triangles) (Eadie & Jurić 2019; Vasiliev & Baumgardt 2021; Wang et al. 2022) and dwarf galaxies (blue diamonds) and the same but devided by $\sqrt{2}$ (violet diamonds) (Li et al. 2021; Hammer et al. 2021; Hammer et al. 2023). Alt text: Outer rotation curve of the halo.

$$\delta V = \left[\frac{\Sigma(V(R)-V_i)w_i}{\Sigma w_i}\right]^{1/2}, \tag{4}$$

where

$$w_i = \exp\left[-\left(\frac{R_i - R}{\delta R}\right)^2\right]\sigma_i^{-2}, \tag{5}$$

and σ_i is the error of the observed value of the i-th data point. We plotted the URC in figure 3 at the same logarithmic radius interval.

In figure 4 we summarize the URCs in linear scales for different radial coverages from the GC to the outermost halo. Figure 5 shows a simultaneous plot of the RC including the SMBH, CMZ, bulge, disk, halo, and outer halo up to ~ 300 kpc, about half way to the Andromeda galaxy, in logarithmic scaling. We name this diagram the "URC26" (unified rotation curve 2026).

3 Deconvolution of URC26 into five mass components

The most basic use of rotation curves is to calculate the mass distribution (Sofue and Rubin 2001). A closer look at URC26 in figure 5 reveals four distinct velocity peaks in the center ($R \sim 0$ pc), near $R \sim 5$ pc, ~ 500 pc, and ~ 5000 pc and an outskirt that extends to $R \sim 300$ kpc corresponding to the dark halo. We decompose the URC26 into the following five mass components.

3.1 Supermassive black hole

The innermost rotation curve at $R \lesssim 1$ pc is represented by the Keplerian law for the massive black hole with $M_{\rm BH} = 4 \times 10^6 M_\odot$ (Ghez et al. 2008; Gillessen et al. 2009):

$$\phi = GM_1/R, \tag{6}$$

and

$$V(R) = V_1/\sqrt{R/a_1} \tag{7}$$

with $V_1 = 131.5$ km s^{-1}and $a_1 = 1$ pc.

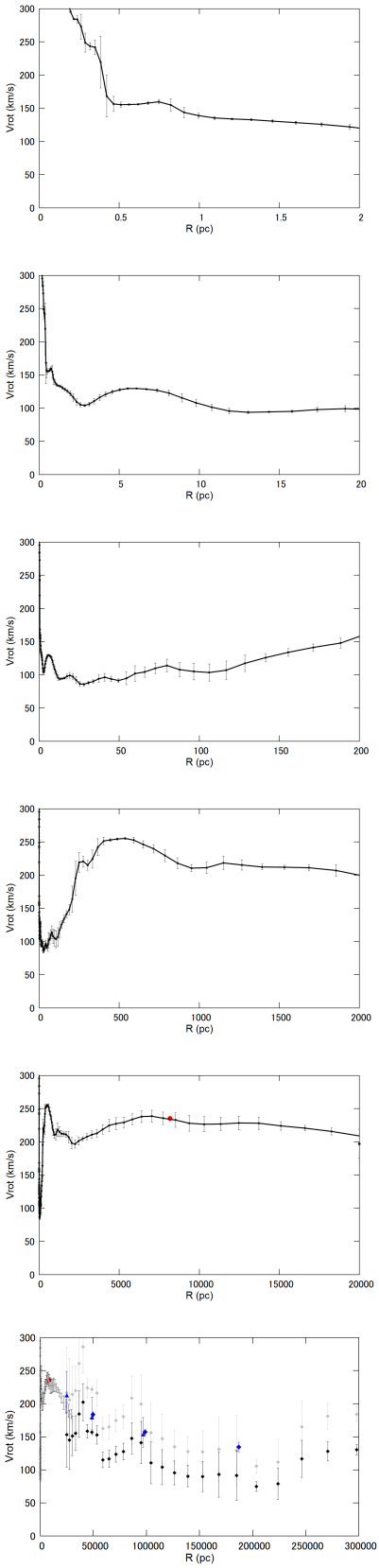

Fig. 4. URC26 by linear scaling for different radial ranges from $R = 0$ (center) to 20 pc, 0 to 200 pc, 0 to 2kpc, 0 to 20 kpc, and 0 to 300 kpc. Alt text: URC26 for various parts of the Galaxy.

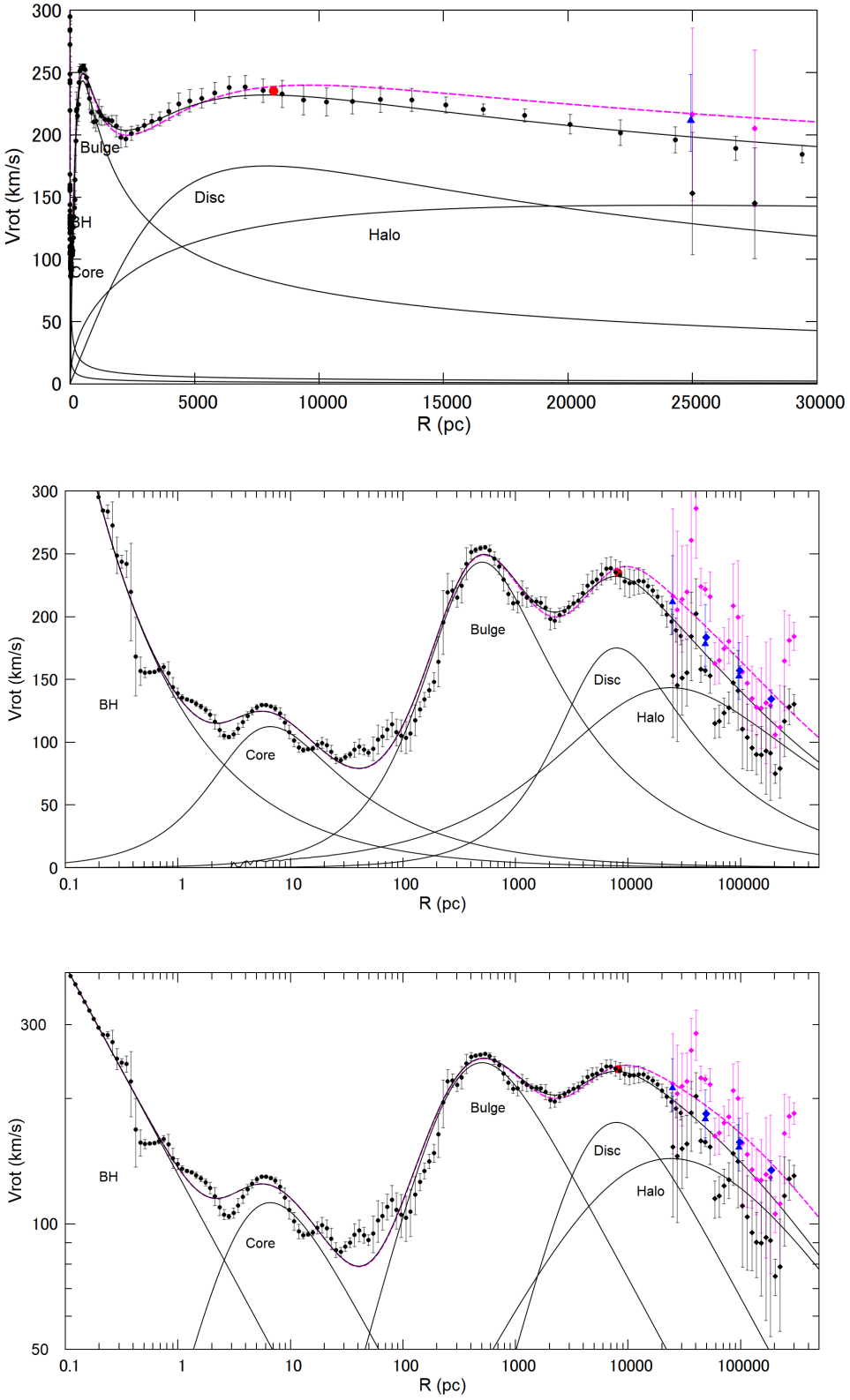

Fig. 5. URC26 from the central SMBH to outer halo up to 30 (top) in linear scaling and to 300 kpc (middle) in semi-logarithmic scaling. Black magenta diamonds are Gaussian running averaged values of the GAIA results for dwarf galaxies with a correction factor $\eta = 1/\sqrt{2}$ (pink diamonds) and $\eta = 1$ (3D velocity, black diamonds), respectively. Big diamonds and triangles are GAIA globular clusters. The lines are calculated RC for the least χ^2 fitting parameters of the URC26 for $\eta = 1/\sqrt{2}$ (black line) and $\eta = 1$ (magenta dash). The innermost Keplerian curve represents the SMBH of $4 \times 10^6 M_\odot$. The core , bulge, and disk are fitted by the Plummer model, while the dark halo is fitted by the NFW model. [Bottom] same, but logarithmic presentation. Alt text: URC26 and fitting result by a calculated RC.

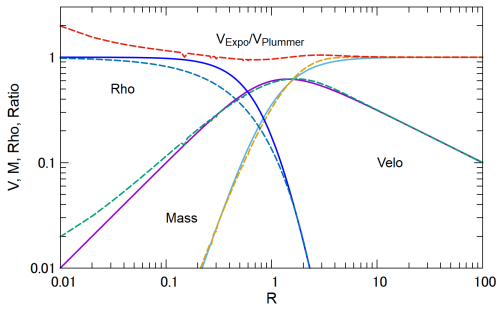

Fig. 6. Radial variations of the rotation velocity, density, mass and the ratio of rotation velocities for the Plummer potential (solid lines) and exponential density profile (dashed lines).

3.2 Core, bulge and disk by Plummer potential

The disk to mid-halo RC at ~ 1 to ~ 15 kpc can be fitted by three components of a core, bulge and disk. We adopt the Miyamoto & Nagai (1975) (MN) potential for each component,

$$\phi_i = GM_i \left[R^2 + (c_i + \sqrt{z^2 + b_i^2})^2\right]^{-1/2}. \quad (8)$$

Since RC provides only the axi-symmetric information at $z = 0$, we approximate it by the following form, which is equivalent to the Plummer potential with $a_i^2 = b_i^2 + c_i^2$:

$$\phi_i = GM_i \left[R^2 + a_i^2\right]^{-1/2} \ (i = 2,\ 3,\ 4). \quad (9)$$

The circular velocity at R is then given by

$$V_i(R) = \sqrt{-R\,\partial\phi^i/\partial R} = V_i x (1 + x^2)^{-3/4}, \quad (10)$$

where $x = R/a_i$, and a_i and V_i are the scale radius and velocity of the i-th component. The total mass of each component is given by

$$M_i = a_i V_i^2 / G. \quad (11)$$

We stress that because gravity has a long range force, the Plummer potential is a good approximation to that of an exponential density distribution, and any similar mass concentrations with sufficiently rapid density decrease, in an accuracy of a few percent. Figure 6 compares the rotation curve calculated for the Plummer potential and for an exponential density sphere with the maximum velocity and radius taken equal.

3.3 Dark halo by NFW profile

The extended outskirts of the URC beyond $R \sim 15$ kpc can be fitted by the dark halo represented by the NFW density profile (Navarro et al. 1997),

$$\rho(x) = \frac{\rho_0}{x(1+x)^2}, \quad (12)$$

where $x = R/h$ with $h = a_5$ being a constant scale radius. Note that the density at $R = h$ is given by $\rho_{\rm DH}(h) = 4\rho_0$. The rotation velocity is given by

$$V(x) = V_5 \sqrt{\frac{\ln(1+x) - x/(1+x))}{x}}, \quad (13)$$

where $V_5 = V_{\rm DH}$ is related to $h = a_5$ and ρ_0 by

$$\rho_0 = \frac{1}{4\pi G}\left(\frac{V_5}{a_5}\right)^2. \quad (14)$$

The dark halo mass inside $R = hx$ is calculated by

$$M(x) = \frac{V_5^2 a_5}{G}\left[\ln(1+x) - \frac{x}{1+x}\right]. \quad (15)$$

We introduce the 'critical DH mass' (White 2001) defined by

$$M_{200} = M(R_{200}), \quad (16)$$

where R_{200} is the 'critical radius' at which the DH density, including dark matter and baryon, hence the core + bulge + disk components, becomes equal to 200 times the critical density of the universe:

$$\rho_{200} = 200\rho_{00}, \quad (17)$$

where

$$\rho_{00} = \frac{3\pi}{8}\frac{H_0^2}{G} \quad (18)$$

is the critical DM+baryon density of the Universe.

3.4 The least χ^2 fit and obtained parameters

We fit the URC26 by superposition of the five mass components as described in the previous section. The scale radius and mass, a_i and V_i, are taken as the free parameters to be fitted with $i = 2$ to 5 showing the core, bulge, disk and halo. We applied the following procedure.

- The central black hole (the first mass component) is fixed to have the observed mass of $4 \times 10^6 M_\odot$ (Ghez et al. 2008) to create the Keplerian RC.
- The initial values of the parameters of the 2nd (core) to 5th (DH) components were given approximately by eye estimates.
- Using the initial parameters, the least χ squares fitting values were searched for the parameters of each component.

The best-fit parameters for the core ($i = 2$), bulge (3), disk (4) and halo (5) components are listed in table 3.5. The error of the fitted parameter is defined by the displacement of the parameter that increases χ^2 by 1 from the minimum.

3.5 Fitted RC and mass distribution

Using the fitted parameters, we calculate the circular velocities and plot the calculated curve as a function of the Galacto-centric distance R for individual components and a total rotation velocity in figure 5. The URC26 with $\eta = 1/\sqrt{2}$ from center to $R \sim 30$ kpc is well reproduced by the calculated RC and the outer halo up to ~ 300 kpc is also reasonably fitted within the errors. However, fitting with $\eta = 1$ significantly overestimates the velocity at $R \sim 10$ to 30 kpc, where accurate GAIA measurements are obtained from the trigonometry of numerous disk stars.

We emphasize that URC26 proves the presence of an outermost massive halo up to $R \sim 300$ kpc, which is reasonably explained by the NFW mass model. However, it does not support the Keplerian decrease in rotation velocity beyond $R \sim 25$ kpc.

We calculate the density profile and the cumulative mass as a function of R using the fitted parameters for $\eta = 1/\sqrt{2}$ and plot them in figure 7. The diagram displays the high density concentration of the mass in the Galaxy from the dark halo to the nucleus, varying over 10 orders of magnitude.

3.6 The dark Halo property

Using equations 16 and 17, we obtain the parameters for the halo as $h \sim 11$ kpc, $R_{200} \simeq 38$ kpc, $M_{200} \sim 3 \times 10^{11} M_\odot$, and $c_{200} = R_{200}/h = 3.5$. Since the density of the core + bulge + disk

Table 1. Fitting parameters for URC26.

Component	Parameter
1. SMBH	V_1 . . . . . 131.5 km s^{-1}
	a_1 . . . . . 1.0 pc ($a_{\rm scale} \sim 0.5$ pc)
	M_1 . . . . . $4.0 \times 10^6 M_\odot$ ‡
Dwarf correction	$\eta = 1/\sqrt{2}$
i =2. Core	V_i . . . . . 181.14 ± 1.25 km s^{-1}
	a_i . . . . . 4.69 ± 0.10 pc
	M_i . . . . . $3.557 \pm 0.077 \times 10^7 M_\odot^*$
3. Bulge	V_i . . . . . 392.35 ± 1.78 km s^{-1}
	a_i . . . . . 357.50 ± 5.43 pc
	M_i . . . . . $0.127 \pm 0.002 \times 10^{11} M_\odot$
4. Disk	V_i . . . . . 282.13 ± 3.71 km s^{-1}
	a_i . . . . . 5589.18 ± 163.26 pc
	M_i . . . . . $1.029 \pm 0.033 \times 10^{11} M_\odot$
5. Dark halo	V_i . . . . . 308.35 ± 3.96 km s^{-1}
	a_i . . . . . 11136.12 ± 688.93 pc
	$(M_i = 2.449 \pm 0.155 \times 10^{11} M_\odot)^*$
	ρ_0 . . . . . 0.539 GeV cm^{-3}
	R_{200} . . . . . 36 kpc †
	c_{200} . . . . . $R_{200}/h = 3.2$
	M_{200} . . . . . $3.0 \times 10^{11} M_\odot$
	$M_{200}^{\rm DM}$ . . . . . $2.0 \times 10^{11} M_\odot$
	$\rho_\odot^{\rm DM}$ . . . 0.244 ± 0.005 GeV cm^{-3}
Dwarf correction	$\eta = 1$
i =2. Core	V_i . . . . . 181.14 ± 1.25 km s^{-1}
	a_i . . . . . 4.69 ± 0.10 pc
	M_i . . . . . $3.557 \pm 0.077 \times 10^7 M_\odot$
3. Bulge	V_i . . . . . 392.58 ± 1.79 km s^{-1}
	a_i . . . . . 358.79 ± 5.47 pc
	M_i . . . . . $0.128 \pm 0.002 \times 10^{11} M_\odot$
4. Disk	V_i . . . . . 294.23 ± 3.68 km s^{-1}
	a_i . . . . . 6310.54 ± 203.79 pc
	M_i . . . . . $1.264 \pm 0.044 \times 10^{11} M_\odot$
5. Dark halo	V_i . . . . . 343.14 ± 4.01 km s^{-1}
	a_i . . . . . 16076.51 ± 1023.68 pc
	$(M_i = 4.379 \pm 0.283 \times 10^{11} M_\odot)^*$
	ρ_0 . . . . . 0.320 GeV cm^{-3}
	R_{200} . . . . . 40.1 kpc †
	c_{200} . . . . . $R_{200}/h = 2.5$
	M_{200} . . . . . $3.8 \times 10^{11} M_\odot$
	$M_{200}^{\rm DM}$ . . . . . $2.8 \times 10^{11} M_\odot$
	$\rho_\odot^{\rm DM}$ . . . 0.276 ± 0.005 GeV cm^{-3}

‡ Ghez et al. (2008)
* $M_i = V_i^2 a_i / G$ (i =2 to 5)
† $H_0 = 71$ km s^{-1}Mpc^{-1}
$\rho_{200} = 200\rho_{00} = 1.87 \times 10^{-26}$g cm^{-3} = 0.0105 GeV cm^{-3}

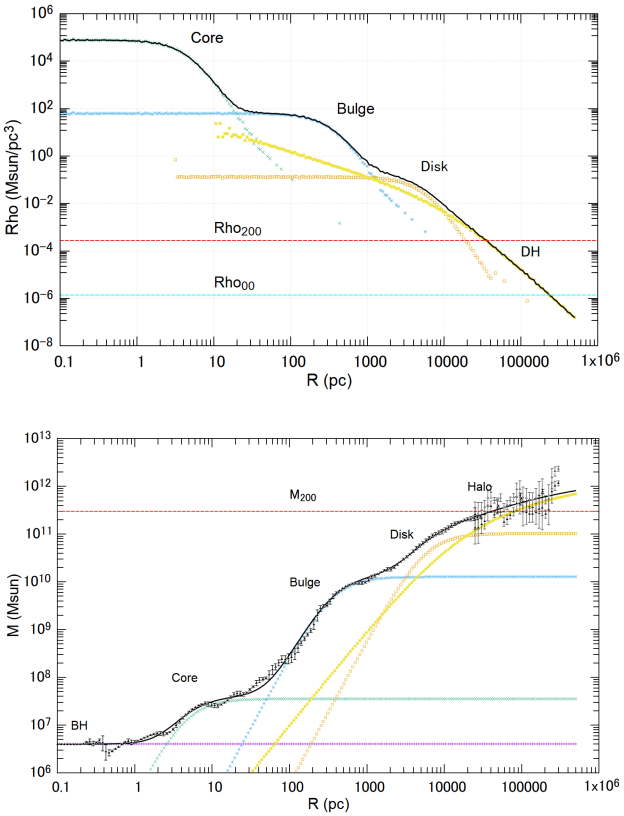

Fig. 7. The density $\rho(R)$ and cumulative mass $M(R)$ calculated for the least-χ^2 URC for $\eta = 1/\sqrt{2}$. Triangles and open triangles with error bars in the lower panel show the mass calculated for individual observed points for $\eta = 1/\sqrt{2}$ (triangles) and $\eta = 1$ (open triangles). Alt text: Density and cumulative mass distributions.

contributes less than 1% of the total density at this radius, the radius R_{200} is correct within a few percent, while the enclosed mass M_{200} calculated for the NFW halo alone is $2.2 \times 10^{11} M_\odot$, much less than the total mass that includes the disk and bulge.

3.7 Scaling relation

The deconvolution of the RC into the components enables us to examine the scaling relation between the scale radius, a_i, and total mass, M_i, of the five mass components of the BH, core, bulge, disk and dark halo. For the BH, we define the scale radius as the radius at which the gravity of the BH dominates that of the core component, i.e., $a_{\rm BH} \sim 0.5$ pc. Figure 8 shows the total masses thus derived against the scale radii of the five components. We find a linear proportionality between the radius and the total mass, which varies by more than six orders of magnitude, and is expressed by $M \sim 10^7 M_\odot (R/1\ {\rm pc})^{1.1}$, as shown by the straight line in the figure.

3.8 Local DM density

The local density of DM is a key parameter for the direct detection experiments of DM. Using equation 12 we calculate the local density of DM at the Sun to be $\rho_\odot^{\rm DM} \simeq 0.24$ GeV cm^{-3} for $\eta = 1/\sqrt{2}$ and ~ 0.28 GeV cm^{-3} for $\eta = 1$. Although the least χ^2 fitting yields small errors, the result depends on the assumed correction

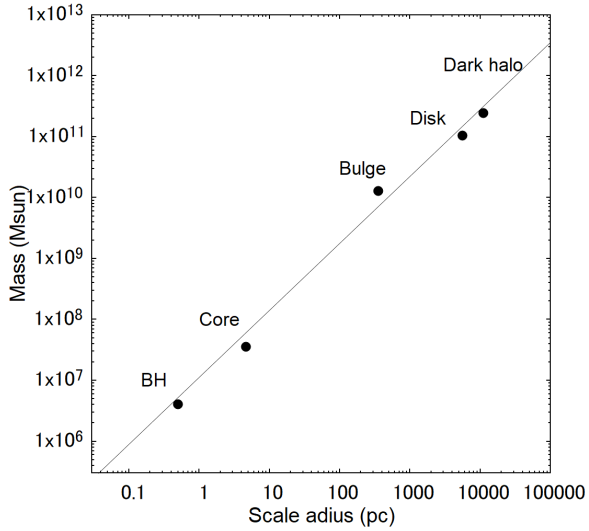

Fig. 8. Scale radius vs total mass of the five mass components of the Milky Way. The radius for BH is approximated by its 'gravity dominant radius'. The upper and lower dots for the DH represent M_{200} (including bulge and disk) and $M_{200}^{\rm DM}$ (DH component alone), respectively. The straight line indicates $M = 10^7 (R/1{\rm pc})^{1.1} M_\odot$. Alt text: Scaling relation among the deconvolved mass components.

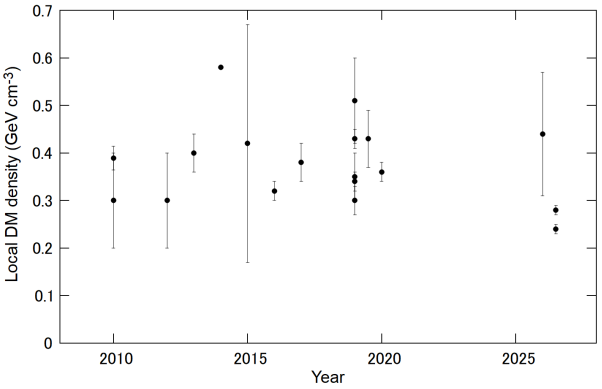

Fig. 9. Measured values of the the local DM density in the decades from Sofue (2020). The most recent values in 2026 are from Söding et al. (2025) and this work at 2026.5.

factor for the dwarf velocity, η, which is taken to be $1sqrt2$ but may vary between ~ 1 and $1/\sqrt{3}$ in equation 2.

In figure 9 we plot the local density values of the DM from the literature taken from Sofue (2020) and the present value that does not include systematic error. The estimated value of $\rho_\odot$ has been nearly constant in the decade, but is re-estimated to be smaller in this work. The general decrease in the value is due to the improvement of the velocity measurements of the outer halo objects by GAIA using stellar objects, globular clusters and dwarf galaxies.

4 Summary

We derived the most completely sampled unified rotation curve of the Milky Way (URC26) from the central super massive black hole to the outer halo of radius ~ 300 kpc, which has the highest resolution and accuracy ever performed. The URC was decomposed into five components of the central black hole with mass of $M_1 = 4 \times 10^6 M_\odot$, the core with $M_2 \simeq 3.5 \times 10^7 M_\odot$ (core), bulge with $M_3 \simeq 1.3 \times 10^{10} M_\odot$ (bulge), disk with $M_4 \simeq 1.06 \times 10^{11} M_\odot$ (disk), and the dark halo with the critical mass of $M_{200} \simeq 3.2 \times 10^{11} M_\odot$ and $M_{200}^{DM} \simeq 2.1 \times 10^{11} M_\odot$ in the critical radius $R_{200} = 35.5$ kpc. The local dark matter density near the Sun due to the dark halo is estimated to be $\rho_\odot^{\rm DM} \sim 0.24$ to 0.28 GeV cm^{-3} .

Acknowledgments

Data analysis was performed at the NAOJ Astronomy Data Center.

Conflict of interests

The author declares that there are no conflicts of interest.

Data availability

The rotation curve used in this paper is downloadable from the PASJ supplementary cite at "http: (to be given by PASJ)" .

References

Braiding, C., Burton, M. G., Blackwell, R., et al. 2015, PASA, 32, e020.
Cubuk, K. O., Burton, M. G., Braiding, C., et al. 2023, PASA, 40, e047.
Dame, T. M., Hartmann, D., & Thaddeus, P. 2001, ApJ, 547, 2, 792.
Eadie, G. & Jurić, M. 2019, ApJ, 875, 2, 159.
Eilers, A.-C., Hogg, D. W., Rix, H.-W., et al. 2019, ApJ, 871, 1, 120.
Ghez, A.M.; Salim, S.; Weinberg, N.N.; et al.ApJ 2008, 689, 1044.
Gillessen, S.; Eisenhauer, F.; Trippe, S.; Alexander, T.; Genzel, R.; Martins, F.; Ott, T. ApJ 2009, 692, 1075.
Ginsburg, A., et al. submitted to MNRAS.
Gravity Collaboration, Abuter, R., Amorim, A., et al. 2019, A&A, 625, L10.
Hammer, F., Wang, J., Pawlowski, M. S., et al. 2021, ApJ, 922, 2, 93.
Hammer, F., Li, H., Mamon, G. A., et al. 2023, MNRAS, 519, 4, 5059.
HI4PI Collaboration, Ben Bekhti, N., Flöer, L., et al. 2016, A&A, 594, A116.
Jiao, Y., Hammer, F., Wang, H., et al. 2023, A&A, 678, A208.
Li, H., Hammer, F., Babusiaux, C., et al. 2021, ApJ, 916, 1, 8.
Longmore, S., et al. 2025, submitted to MNRAS
Miyamoto, M. & Nagai, R. 1975, PASJ, 27, 533.
Navarro, J.F.; Frenk, C.S.; White, S.D.M.ApJ. 1997, 490, 493.
Poggiani, R. 2025, Galaxies, 13, 3, 65.
Reid, M. J., Menten, K. M., Brunthaler, A., et al. 2019, ApJ, 885, 2, 131.
Salucci, P.A&Ap. Rev. 2019, 27, 2.
Söding, L., Bartel, R. L., & Mertsch, P. 2025, MNRAS, 542, 4, 2987.
Sofue, Y. 2012, PASJ, 64, 75.
Sofue, Y. PASJ 2013, 65, 118.
Sofue, Y.PASJ 2017, 69, R1.
Sofue, Y.; Rubin, V.ARA&Ap 2001, 39, 137.
Sofue, Y. 2020, Galaxies, 8, 37.
Sofue, Y.; Honma, M.; Omodaka, T. PASJ 2009, 61, 227.
Sofue, Y. & Kohno, M. 2025, PASJ, 77, 6, 1335.
Sofue, Y., Oka, T., Longmore, S. N., et al. 2025, arXiv:2504.03331.
Sylos Labini, F. 2024, ApJ, 976, 2, 185.
Umemoto, T., Minamidani, T., Kuno, N., et al. 2017, PASJ, 69, 78
VERA Collaboration, Hirota, T., Nagayama, T., et al. 2020, PASJ, 72, 4, 50.
Walker, D. L., et al. 2025, submitted to MNRAS
Vasiliev, E. & Baumgardt, H. 2021, MNRAS, 505, 4, 5978.
Wang, J., Hammer, F., & Yang, Y. 2022, MNRAS, 510, 2, 2242.
White, M. 2001, A&A, 367, 27.